Ultrafast Metal Oxide Reduction at Pd/PdO_2 Interface Enables One-Second Hydrogen Gas Detection Under Ambient Conditions

Xin Geng,[†,‡] Shuwei Li,[§,∥,Σ‡] Zhi Mei,[†] Dongsheng Li,[Δ] Liang Zhang,[§,∥,Σ*] and Long Luo[†,*]

[†] Department of Chemistry, Wayne State University, Detroit, Michigan 48202, United States

[§] Center for Combustion Energy, Tsinghua University, Beijing 100084, China

[∥] School of Vehicle and Mobility, Tsinghua University, Beijing 100084, China

[Σ] State Key Laboratory of Automotive Safety and Energy; Beijing 100084, China

[Δ] Physical and Computational Sciences Directorate, Pacific Northwest National Laboratory, Richland, WA 99352, USA

ABSTRACT: Here, we report a Pd/PdO_x sensing material that achieves 1-s detection of 4% H_2 gas (i.e., the lower explosive limit concentration for H_2) at room temperature in air. The Pd/PdO_x material is a network of interconnected nanoscopic domains of Pd, PdO, and PdO_2. Upon exposure to 4% H_2, PdO and PdO_2 in the Pd/PdO_x can be immediately reduced to metallic Pd, generating over a >90% drop in electrical resistance. The mechanistic study reveals that the Pd/PdO_2 interface in Pd/PdO_x is responsible for the ultrafast PdO_x reduction. Metallic Pd at the Pd/PdO_2 interface enables fast H_2 dissociation to adsorbed H atoms, which is otherwise the rate-determining step on PdO_2, significantly lowering the PdO_2 reduction barrier. In addition, the interconnectivity of Pd, PdO, and PdO_2 in Pd/PdO_x facilitates the reduction of PdO. The 1-s response time of Pd/PdO_x under ambient conditions makes it an excellent alarm for the timely detection of hydrogen gas leaks.

INTRODUCTION

Hydrogen (H_2) is an attractive fuel option for transportation and electricity generation applications because it is clean—water is the only product when used in a fuel cell—and can be produced from a variety of resources such as natural gas, biomass, or by water splitting using renewable power.[1] Because H_2-air mixtures are highly explosive, the wide adoption of hydrogen fuel requires immediately detecting the H_2 leakage at the locations where H_2 is produced, stored, transported, and used.[2] Hence, the U. S. Department of Energy (DOE) has set target specifications for H_2 safety sensor R&D in terms of the measurement range (0.1% to 10%), operating temperature (-30°C to 80°C), response time (1 s), gas environment (ambient air, 10% -98% relative humidity), lifetime (10 years), and resistance to interferences (e.g., hydrocarbons).[3] Among all the metrics, the response time ($t_{response}$) of 1 s in ambient air is the most challenging yet crucial one.[4] Only a few H_2 sensors have been reported to respond to 4% H_2 within 1 s (**Table 1**).[5-15] These sensors can be generally summarized as the following two types: nanogap and plasmonic. For the nanogap sensors, there are nanoscopic gaps in the Pd sensing material. Upon exposure to H_2, Pd reacts with H_2 to form PdH_x. The expanded volume of PdH_x relative to Pd closes the nanogaps, resulting in a sudden electrical resistance drop. When the nanogaps are sufficiently small (< 50 nm), $t_{response}$ can be as short as 75 ms.[8] For the plasmonic sensors, the sensor response arises from the shift of the localized surface plasmon resonance peak of Pd-based nanoarchitectures upon H_2 absorption by Pd. Their fast response was achieved by tailoring the volume-to- surface ratio in concert with reducing the apparent activation energy for H_2 absorption by engineering the metal-polymer coating interface [10, 11] and the sensing material composition[5, 10, 13, 14]. However, in these prior works, the 1-s response time was achieved either in an inert gas environment (e.g., N_2 and Ar) or under vacuum, not in the ambient air as required by the DOE. Pd-based sensors typically show degraded performance with reduced sensitivities and sluggish sensing speeds in the ambient air relative to the inert gas environment because O_2 competes with H_2 for surface sites, impeding H_2 reactions with Pd.[2, 16]

Table 1. Summary of the room-temperature hydrogen sensors with a response time ($t_{response}$) ≤ 1s in the literature.

Materials	Transducer platform	$t_{response}$ (s)	Background environment	Ref.
PdAu NP @PTFE/PMMA	Optical	1	Vacuum	[10]
PdAuCu NP	Optical	0.4	Vacuum	[14]
TaPd thin film	Optical	0.5	Ar	[5]
POSS/Pd NP composite	Optical	1	Ar	[11]
PdCo alloy	Optical	0.85	N_2, Vacuum	[13]
Pd mesowire	Electrical	0.075	N_2	[8]
Pd nanogap	Electrical	1	N_2	[9]
Pd nanogap	Electrical	1	N_2	[7]
Pd ultrathin film	Electrical	0.068	N_2	[12]
Pd NP on SiO_2 film	Capacitive	1	N_2	[6]
Pd/PdO_x	Electrical	1	Air	This work

Generally, there are two prerequisites to achieve ultrafast gas detection: first, rapid reaction kinetics between sensing material and gas analyte, and second, rapid transduction of the above reaction into a physical character that can be detected.[17] In this work, we chose to explore the hydrogen reduction of metal oxides to realize the 1-s detection of 4% H_2 under ambient conditions because (1) metal oxide reduction is autocatalytic,[18] meaning that once the reaction is initiated, it would self-accelerate and quickly complete; (2) O_2 typically binds weakly to pure metal oxides, reducing its adverse impact on the H_2 reactions with the sensing materials; and (3) the reduction of non-conducting or semiconducting metal oxides to conductive metals yields an instant and substantial electrical resistance drop, enabling effective and rapid signal transduction. However, to initiate the direct reduction of metal oxides such as PdO, CuO, Cu_2O, Ag_2O, and NiO by H_2 is difficult at room temperature and often requires elevated temperatures to complete.[18-23] For example, the apparent activation energy for directly reducing Cu_2O by H_2 is about 27.4 kcal/mol, and the reduction process took ~180 min to complete, even at 230 °C. Introducing a metal (e.g., Pt, Pd, Ru)/metal oxide interface is a possible solution to accelerating the initial metal oxide reduction kinetics. It has been reported that these metal/metal oxide interfaces create highly reactive oxygen species due to the charge transfer between metal and oxide.[24-34] Moreover, the metal/metal oxide interface allows facile migration of atomic hydrogen readily dissociated by metals to metal oxides in close proximity (i.e., hydrogen spillover).[21, 35-37] The reactive oxygen species and atomic hydrogen react quickly, resulting in the rapid reduction of metal oxide. Thus, tailoring the metal/metal oxide interface offers a unique opportunity to accomplish the challenging 1-s detection of H_2 under ambient conditions by rendering ultrafast metal oxide reduction kinetics.

Herein, we report a Pd/PdO_x material with ultrafast metal oxide reduction kinetics, enabling 1-s detection of 4% H_2 under ambient conditions. The Pd/PdO_x material was prepared by electrophoretically depositing Pd nanoparticles (NPs) onto a sensor substrate followed by *in situ* partial electrochemical oxidation of Pd to PdO_x, forming a network of interconnected nanoscopic domains of Pd, PdO, and PdO_2. Upon exposure to 4% H_2, PdO_2 is wholly reduced to metallic Pd, and PdO is partially reduced within just 1 s, leading to a >90% drop in electrical resistance. The mechanistic study reveals that the Pd/PdO_2 interface is responsible for the fast reduction. More specifically, the presence of Pd shifts the rate-determining step for the PdO_x reduction from dissociative chemisorption of H_2 molecules on PdO_2 to the diffusion of adsorbed H atom on PdO_2 by first dissociating H_2 on metallic Pd, significantly lowering the activation energy barrier of PdO_2 reduction from ~0.9 eV to ~0.6 eV.

RESULTS AND DISCUSSION

Pd/PdO$_x$ sensors preparation and characterization

Pd/PdO$_x$ sensors were fabricated in one step by electrophoretically depositing citrate-capped Pd NPs onto a sensor substrate at a high potential of 10 V using a three-electrode setup, where Ag/AgCl/sat. KCl was used as the reference electrode and a Pt foil as the counter electrode (**Figure 1A** and **S1**). Under the high potential of 10 V, the citrate ligands on Pd NPs were oxidatively removed once the NPs landed on the electrode, as evidenced by the disappearance of the C1s peak at 288 eV in the X-ray photoelectron spectrum (XPS) of as-synthesized Pd/PdO$_x$ (**Figure S2**). The loss of ligand protection caused the NPs to aggregate into a porous network (NP size = 2.7± 0.3 nm and wire width = 6.6 ± 0.8 nm, **Figures 1B-D**, **S3**).

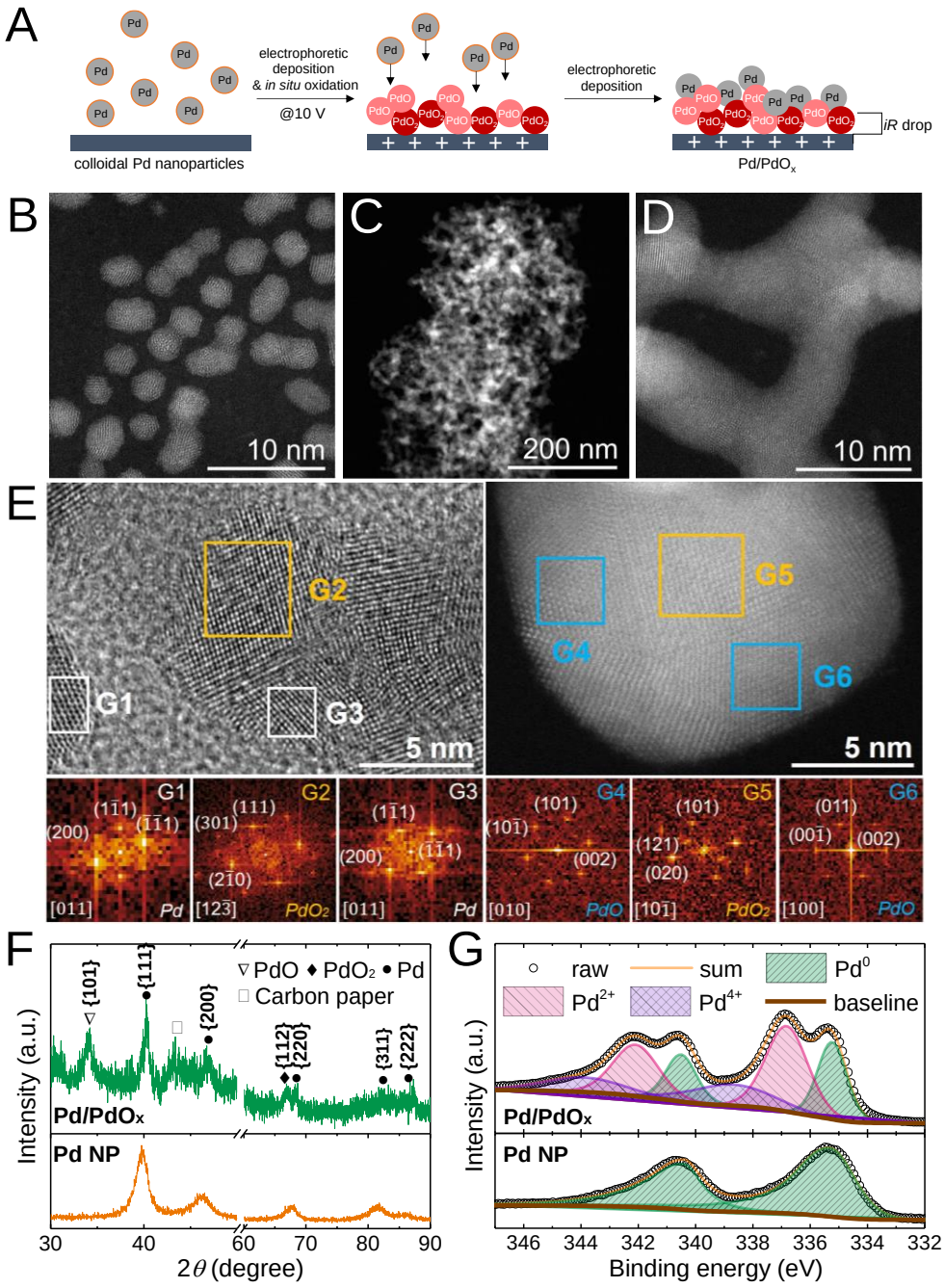

Figure 1. (A) Schematic illustration of the preparation of Pd/PdO$_x$ sensors by electrophoretic deposition and partial in situ oxidation of Pd NPs. (B-D) High−Angle Annular Dark−Field Scanning Transmission Electron

Microscopy (HAADF−STEM) images of B) Pd NP; C) and D) Pd/PdO_x electrophoretically deposited at 10 V (labeled as Pd/PdO_x). E) Representative high-resolution TEM and STEM images of Pd/PdO_x, and the corresponding Fast Fourier Transformed (FFT) diffraction patterns for the color-coded regions. White, yellow, and blue correspond to cubic Pd, tetragonal PdO, and tetragonal PdO_2. F) Powder X-ray diffraction (PXRD) patterns of Pd NPs and Pd/PdO_x. The peak assignments were based on the standard PDF cards of No. 00-046-1043 (cubic Pd), No. 00-041-1107 (tetragonal PdO), No. 00-034-1101 (tetragonal PdO_2). G) X-ray photoelectron spectroscopy (XPS) showing the Pd 3d region of Pd NPs and Pd/PdO_x.

Analysis of high-resolution transmission electron microscopic (HRTEM) images reveals that the deposited Pd material is composed of interconnected nanoscopic domains of Pd, PdO, and PdO_2, as supported by the fast Fourier transform (FFT) diffraction patterns that match well with cubic Pd, tetragonal PdO, and tetragonal PdO_2 (**Figure 1E**). The powder X-ray diffraction (PXRD) pattern also exhibits the signature peaks of Pd, PdO, and PdO_2, for example, the {111} peak for Pd, the {101} peak for PdO, and the {112} peak for PdO_2 in **Figure 1F**. As a reference, the Pd NP precursor only shows the PXRD peaks of Pd. Moreover, the XPS measurements demonstrated that a new Pd $3d_{5/2}$ peak emerged at ~337eV (**Figure 1G**), consistent with the PdO phase.[38] Numerical fitting of the XPS data reveals that Pd/PdO_x contains 29% Pd, 48% PdO, and 23% PdO_2 (**Table S1**). All the structural characterization data have confirmed the partial Pd oxidation to PdO and PdO_2 during the electrophoretic deposition process. The formation of PdO and PdO_2 is expected because our electrode potential is higher than the equilibrium potential of a hydrated PdO and hydrated PdO_2 mixture (~1.23 V vs. standard hydrogen electrode).[39] However, according to the Pourbaix diagram for Pd, Pd should not be thermodynamically stable at 10 V and pH= ~1 (experimentally measured near the sensor substrate during electrodeposition).[40] The co-existence of Pd, PdO, and PdO_2 phases in Pd/PdO_x is possible because the poor conductivity of PdO and PdO_2 lowers the actual potential applied on some Pd NPs, avoiding the total conversion of Pd to PdO_x.

H_2 sensing performance

The performance of Pd/PdO_x sensors was tested using a homebuilt apparatus (**Figure S4)**. The response time ($t_{response}$) was defined as the time required for the signal to vary by 90%. Strikingly, the Pd/PdO_x sensor resistance drops steeply by over 90% in 1 s upon exposure to 4% H_2 in ambient air (**Figure 2A**). The XRD and XPS analysis of the Pd/PdO_x sensor after H_2 exposure shows the complete reduction of PdO_2 to Pd and ~65% reduction of PdO to Pd (**Figure S5, Table S2**), confirming that the rapid PdO_x reduction is responsible for the ultrashort $t_{response}$ and high sensor response. The sensor does not recover after H_2 removal because PdO_x reduction is irreversible. $t_{response}$ becomes longer while sensor response becomes smaller with decreasing H_2-concentration (C_{H2}) (**Figures 2A, S6**). Relative humidity has an impact on the sensor performance: $t_{response}$ is 1 s at a humidity level ≤ 25% but gets longer at higher humidity levels (for example, ~4 s at 50%) due to the competitive adsorption between water vapor and H_2 onto the sensor surface. However, relative humidity did not change the sensor response (**Figures 2B, S7**).

Next, we assessed the cross-sensitivity of the Pd/PdO_x sensor toward 32 different interference gases, including CO, NO_2, NO, SO_2, H_2S, NH_3, and various organic gas and vapors such as natural gas, hexane, benzene, formaldehyde, methanol, etc. All interference gases have a concentration of 4% in air, except for H_2S (0.4 ppm), NO_2, NO, and SO_2 (4 ppm for each), and ethylene (40 ppm). The interference test results show that the Pd/PdO_x sensors only exhibit weak cross-sensitivity (~10 to 30%) toward CO, CH_4, and NH_3, and negligible response (<5%) to other interference gases, relative to H_2 (**Figures 2C, S8**). The weak cross-sensitivity to CO and CH_4 is because CO and CH_4 can partially reduce PdO_x to Pd, but to a much less extent than H_2. Interestingly, the reactivity of Pd/PdO_x toward CO and CH_4 was also different: CO reacted mostly with PdO, whereas CH_4 selectively reacted with PdO_2 (**Figure S9, Table S3**). These findings are consistent with the literature reports that different Pd-O species exhibit different reactivities toward CO and CH_4.[38, 41, 42] Pd, PdO, or a Pd/PdO mixed phase is not active for CH_4 activation at room temperature.[38] In comparison, adsorbed O on metallic Pd could be reduced by CO within a few minutes already at a temperature as low as 223 K, while the more deeply oxidized Pd was much less reactive and required an elevated temperature.[42] Because of such reactivity differences, the Pd/PdO_x sensor could still show a rapid (~3 s) and significant response (> 70%) to 4% H_2 even after being exposed to 4% CO for 5 min (**Figure 2D**), indicating the excellent CO-poisoning tolerance of the Pd/PdO_x sensor. For NH_3, the composition of Pd/PdO_x did not show a noticeable change after the test (**Figure S9, Table S3**), suggesting that the sensor

response did not arise from PdO_x reduction. The sensor resistance increased after introducing NH_3 and partially recovered once NH_3 was removed (**Figure S8**), which is characteristic of a *p*-type semiconductor gas sensor in response to a reducing gas analyte such as NH_3,[43] consistent with the *p*-type nature of PdO.[44, 45] It is also worth noting that the reaction kinetics between CO, CH_4, and NH_3 with Pd/PdO_x is much slower than H_2, taking at least ten times longer to complete (**Figure S8**). Moreover, our one-step electrophoretic synthesis simplifies the sensor fabrication, undoubtedly lowering the production cost and ensuring reproducibility among devices. Indeed, we tested five independently prepared Pd/PdO_x sensors and found a remarkably low device-to-device sensor response variation of <3% and a constant $t_{response}$ of 1 s (**Figure 2E**).

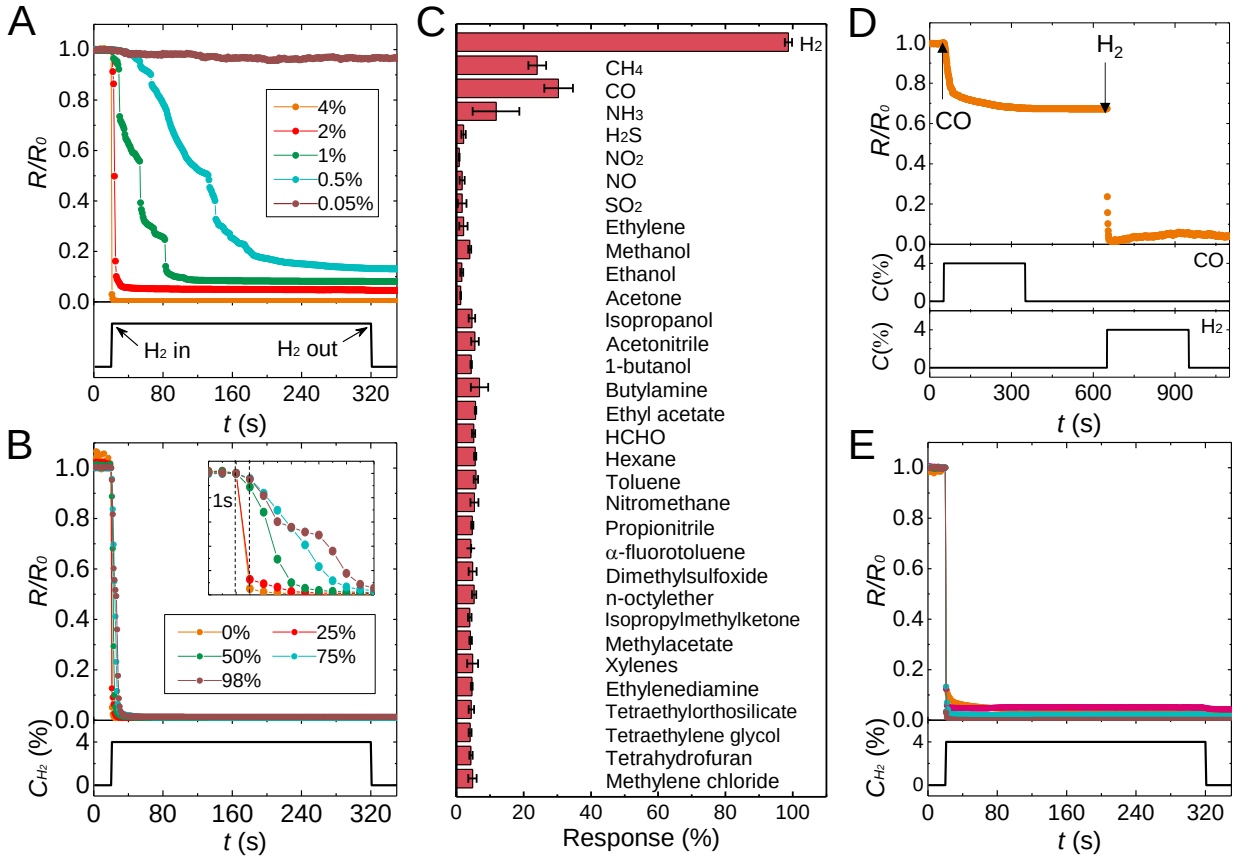

Figure 2. A) Dynamic sensing resistance curves of Pd/PdO_x in response to H_2 at different concentrations (0.05%–4%) at room temperature in air. The data acquisition rate is 1 Hz, meaning each data point is 1 s. R_0 is the baseline resistance. B) Humidity dependence of Pd/PdO_x towards 4% H_2 with humidity ranging from 0% to 98% at room temperature. The insert shows the response-recovery curve in the first ten seconds upon exposure to H_2 gas. C) The percentage change of sensor response upon exposure to 32 different interference gases. The concentrations of interference gases are 4%, except for ethylene (40 ppm), NO_2 (4 ppm), NO (4 ppm), SO_2 (4 ppm), H_2S (0.4 ppm). D) The CO poisoning test by exposing the Pd/PdO_x sensor to 4% CO and 4% H_2 in succession. E) Dynamic sensing resistance curves of 5 independently prepared Pd/PdO_x sensors in response to 4% H_2.

Mechanistic understanding

The exceptionally rapid response of Pd/PdO_x sensors to H_2 undoubtedly results from the ultrafast PdO_x reduction kinetics. However, due to the complex structure of Pd/PdO_x, it is challenging to precisely identify the active sites that are responsible for the fast reduction. Thus, we started the mechanistic study by investigating the composition effect on $t_{response}$. The composition of Pd/PdO_x was varied by applying different electrode potentials during electrophoretic deposition. The XPS results show that the Pd/PdO_x materials prepared under 1 V, 2 V, 5 V, and 10 V were all composed of Pd, PdO, and PdO_2 and citrate ligands were

also removed during electrosynthesis for all samples (**Figures S2, S10**). As the electrode potential was increased from 1 V to 10 V, the Pd^0 content gradually decreased from 43% to 29%, PdO_2 increased from 12% to 23%, and PdO stayed at ~50% (**Table S1**). Upon exposure to 4% H_2 in air, all Pd/PdO_x sensors exhibited a substantial resistance decrease due to the PdO_x reduction to metallic Pd (**Figures 3A, S11-12,** and **Table S2**). However, there are two noticeable differences between the response curves of the Pd/PdO_x sensors prepared at 5 and 10 V and those prepared at 1 V and 2 V (**Figure 3A**). First, $t_{response}$ of the 1 V and 2 V sensors (6 s and 11 s, respectively) are much longer than the 1 s of the 5 V and 10 V ones. Second, their responses are also smaller. Because the compositional differences among these samples were mainly from Pd and PdO_2, it is reasonable to hypothesize that Pd and PdO_2 are the two critical ingredients in Pd/PdO_x to achieve fast reduction.

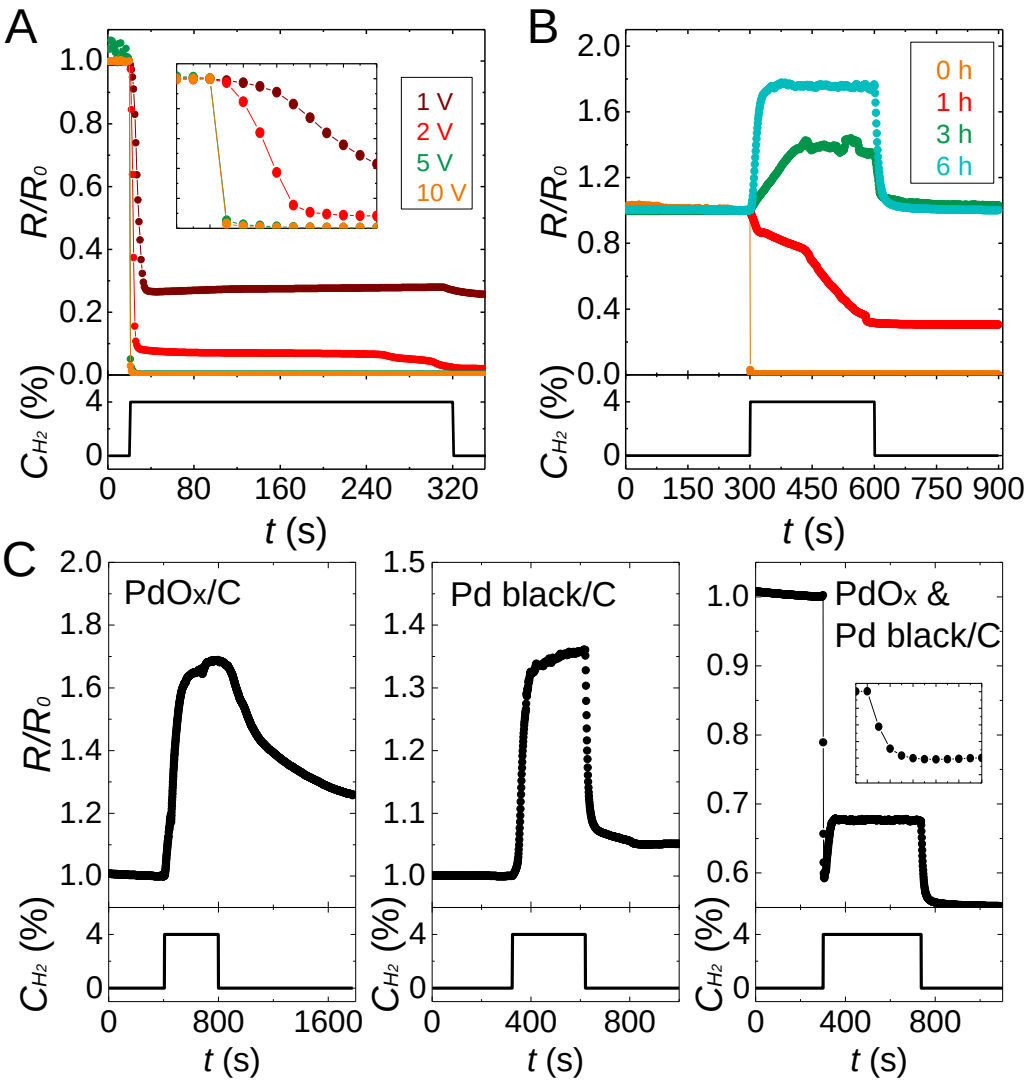

Figure 3. A) Dynamic sensing resistance curves of Pd/PdO_x prepared by electrophoretic deposition using various potentials of 1-10 V towards 4% H_2. B) Dynamic sensing resistance curves at 4% H_2 for the Pd/PdO_x samples after thermal treatment at 400°C for 1, 3, and 6 h in air. C) Dynamic sensing resistance curves of commercial Pd oxide (PdO_x/C), Pd black, and the physical mixture of the two (PdO_x&Pd black/C) to 4% H_2. The inset shows the expanded view in the first ten seconds upon exposure to H_2.

To test our hypothesis, we first thermally annealed the Pd/PdO_x in air to eliminate metallic Pd by oxidizing it to PdO and PdO_2. After thermal treatment for 6 hours, Pd in Pd/PdO_x was converted to PdO and PdO_2 (PdO: 67.1 and PdO_2: 32.9%, **Figure S13, Table S4**). The sensing response of thermally treated Pd/PdO_x

was completely different from that of the initial Pd/PdO_x. For the 6-hour sample, the sensor showed the typical behavior of a *p*-type semiconductor gas sensor: the electrical resistance increased in response to H_2 with $t_{response}$ of 32 s at 4% H_2 (**Figure 3B**). PdO_x was also not reduced to metallic Pd after exposure to 4% H_2 for 5 min (**Figure S14, Table S4**). For Pd/PdO_x samples with 1- and 3-hour-long thermal treatment, their sensing behaviors lay in between semiconductor sensing and metal oxide reduction sensing (**Figure 3B**). The same *p*-type semiconductor sensing characteristics and no oxide reduction were observed for commercial Pd oxide (PdO_x/C) with a similar chemical composition of PdO: 72.7% and PdO_2: 27.3% (**Figures 3C, S16,** and **Table S5-S6**). The above observations are consistent with the literature report that the onset of the reduction of pure metal oxides such as PdO occurs at temperatures higher than 500–700 K.[46] We also carried out a control experiment by annealing Pd/PdO_x in Ar at 400ºC for 6 h. The annealed sample largely retained its composition and showed similar metal oxide reduction sensing behavior as the untreated sensors (**Figure S15, Table S4**). The above results show that the presence of metallic Pd is critical to initiating the rapid reduction of PdO_x at room temperature.

Next, we attempted to prepare Pd/PdO with similar morphology as Pd/PdO_x at potentials lower than 1 V to prove the essential role of PdO_2 in the rapid PdO_x reduction. However, we found the incomplete removal of citrate ligands from the Pd surface during the electrophoretic deposition, leading to inconclusive results. Therefore, we turned to the commercial ligand-free Pd black containing 46.5% Pd and 53.5% PdO (Pd black/C, **Figure S16,** and **Table S5**). The Pd black/C sensor exhibited *p*-type semiconductor sensing behavior (**Figure 3C**), the same as other Pd/PdO sensors reported in the literature.[47, 48] The XPS analysis revealed that the PdO content of Pd black did not change after exposure to 4% H_2 (**Figure S16, Table S6**), indicating that H_2 reduction of PdO is insignificant even in the presence of Pd^0 at room temperature.

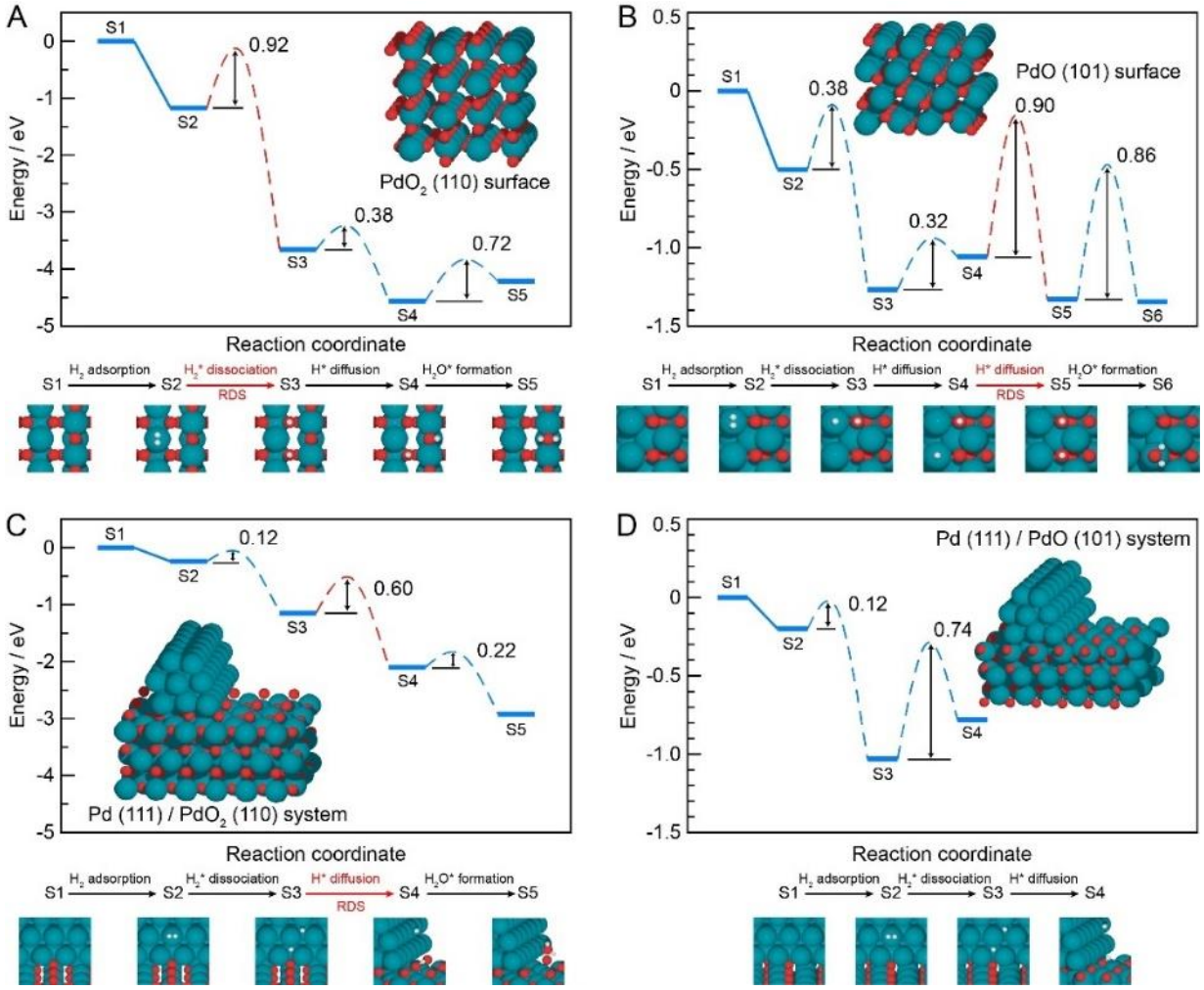

Figure 4. DFT-calculated energy profiles for hydrogen reduction of PdO and PdO_2 to form water on (A) PdO_2 (110) surface, (B) PdO(101) surface, (C) Pd NP on a PdO_2 surface containing a Pd(111)/PdO_2(110) interface, and (D) Pd NP on a PdO surface containing a Pd(111)/PdO(101) interface. The configurations at the bottom show a schematic representation of reactants and products in every reaction step. Cyan, red, and white balls represent Pd, O, and H atoms. RDS stands for the rate-determining step.

Thus far, our compositional study has shown that neither Pd/PdO nor PdO/PdO_2 could effectively react with 4% H_2 at room temperature to be reduced to Pd, supporting our hypothesis that Pd and PdO_2 are responsible for the rapid reduction. Certainly, we did not consider the possible contributions of the unique nanostructures of Pd/PdO_x to the rapid oxide reduction at room temperature, which could be significant. Thus, to assess whether the unique nanostructure of Pd/PdO_x (i.e., interconnected nanodomains of Pd, PdO, and PdO_2) indeed plays a critical role in the rapid reduction of PdO_x, we prepared a composite of Pd, PdO, PdO_2 by physically mixing commercial Pd black and PdO_x/C. The PdO_x&Pd black/C composite has a similar composition (Pd: PdO: PdO_2= 23%: 63%:14%) as our Pd/PdO_x material but without the nanoscopic structural features. Intriguingly, the PdO_x&Pd black/C sensor showed a similar rapid resistance drop by 40% in the first 3 s as the Pd/PdO_x sensor (**Figure 3C**). XPS result shows that the resistance drop was exclusively caused by the reduction of PdO_2 to metallic Pd, and the PdO content did not change (**Figure S16** and **Table S6**). After the initial 3 s, the unreduced PdO in PdO_x&Pd black/C led to the *p*-type semiconductor sensing response (**Figure 3C**). These results indicate that (1) when Pd and PdO_2 are adjacent either via grain boundaries as in Pd/PdO_x samples (**Figure 1E**) or simply physical contact as in the PdO_x&Pd black/C, they can trigger the rapid reduction; and (2) the interconnected nanodomains of Pd, PdO, and PdO_2 enables the reduction of PdO by 4% H_2 at room temperature which would otherwise not occur.

To understand why the Pd/PdO_2 combination significantly accelerates the PdO_x reduction whereas Pd/PdO does not, we carried out density functional theory (DFT) calculations of the energy profiles for metal oxide reaction with H_2 on PdO_2(110) surface, PdO(101) surface, Pd(111)/PdO_2(110) interface and Pd(111)/PdO(101) interface (**Figure 4**). The calculated energy profiles in **Figures 4A**-**B** show that the PdO_2(110) and PdO(101) surfaces have different rate-determining steps (RDS): H_2* dissociation for PdO_2(110) and H* diffusion for PdO(101). For the Pd(111)/PdO_2(110) interface, the sluggish H_2* dissociation on PdO_2(110) is bypassed by the alternative low-barrier pathway on Pd (111) surface (H_2* dissociation energy: 0.92 eV → 0.12 eV, **Figure 4C**). The energy barriers for H* diffusing from Pd (111) to PdO_2 (110) surface, and subsequent H_2O* formation process were 0.60 and 0.22 eV, respectively (S3 → S4 and S4 → S5 in **Figure 4C**). Therefore, the RDS for PdO_2 reduction switches from H_2* dissociation to H* diffusion when Pd/PdO_2 interface is present. We have also found another possible H* diffusion pathway from Pd to PdO_2 via a bridging binding geometry of H* at the Pd/PdO_2 interface, which could further reduce the diffusion energy barrier to 0.40 eV (**Figure S17**). In contrast, although accelerated H_2* dissociation on Pd also took place at the Pd(111)/PdO(101) interface, the H* diffusion remains as the RDS for PdO reduction (**Figure 4D**), suggesting that the reduction kinetics of PdO (101) benefit much less from the Pd/PdO interface. The above DFT results clearly explain the essential role of Pd/PdO_2 interface in achieving ultra-fast metal oxide reduction, in excellent agreement with experimental observation in **Figure 3**.

CONCLUSION

In conclusion, we reported a Pd/PdO_x material with ultrafast hydrogen reduction kinetics, enabling 1-s detection of 4% H_2 in ambient air. The mechanistic study reveals that the Pd/PdO_2 interface in Pd/PdO_x should be responsible for the rapid reduction of PdO_x. The presence of metallic Pd allows rapid H_2 dissociation to adsorbed H atoms, overcoming the RDS in PdO_2 reduction. In contrast, because the RDS of PdO reduction is the adsorbed H atom diffusion on PdO, not the H_2 dissociation, PdO reduction does not benefit from the facile H_2 dissociation at the Pd/PdO interface. However, the interconnectivity of Pd, PdO, and PdO_2 in Pd/PdO_x enables the reduction of PdO, which would otherwise not occur. Due to the irreversible nature of PdO_x reduction to Pd, the Pd/PdO_x sensor does not recover after H_2 exposure and thus can only be used as a H_2 alarm. We are now exploring other combinations of metal and high-valance metal oxide to develop 1-s response time H_2 alarms that can be "reset" by regenerating the metal oxide after the alarm is triggered.

METHODS

Preparation of Pd NPs. Pd NPs were synthesized using a modified approach in the literature. Briefly, 20 mL aqueous solution of 0.14 mmol potassium tetrachloropalladate(II) (Sigma Aldrich) was added in 400 mL of DI water at ambient temperature. After one minute, 10 mL aqueous solution of 0.84 mmol sodium citrate tribasic dehydrate (Sigma Aldrich) was added. After waiting for another one minute, 5 mL of the freshly prepared ice-cold aqueous mixed solution of 0.14 mmol sodium borohydride (Sigma Aldrich) and 0.56 mmol sodium citrate tribasic dehydrate was added and the reaction lasted for another 10 min. The whole reaction is carried out under magnetic stirring at 700 rpm. Before electrophoretic deposition, the as-synthesized Pd NP solution was concentrated using a rotary evaporator by 2-fold to a final volume of ~200 mL and Pd NP concentration of ~1.0 μM.

Estimation of the Pd NP concentration. The concentration of the Pd NP solution was calculated to be ~1.0 μM as follows:

The volume of a Pd NP: $V_{Pd\ NPs} = \frac{4}{3} \times \pi \times r^3 = 10.3\ nm^3$

(the average size of 2.7 nm derived from STEM images)

The volume of a fcc Pd unit cell found in the PDF card No. 00-046-1043: $V_{Pd\ unit\ cell} = 0.059\ nm^3$

The number of unit cells in one Pd NP: $N_{cell} = V_{Pd\ NPs}/V_{Pd\ unit\ cell} \approx 175$

The total number of Pd atoms in one Pd NP: $N_{Pd} = 4 \times N_{cell} \approx 700$

The concentration of Pd atoms in the Pd NP solution: $C_{Pd} = n_{Pd}/V_{Pd\ solution} \approx 0.7\ mM$

The Pd NP concentration: $C_{Pd\ NPs} = C_{Pd}/N_{Pd} \approx 1.0\ \mu M$

Preparation of Pd/PdO$_x$ sensors. The 1.0 μM Pd NP solution was used for electrophoretic deposition using a CHI 650E potentiostat, where a sensor substrate as the working electrode, a Pt foil (~385 mm^2) as the counter electrode, an Ag/AgCl electrode in saturated KCl as the reference electrode (**Figure S1**). The sensor substrate is an electrical insulator made of a sintered alumina plate with interdigitated Pt electrodes on one side. The distance between two neighboring Pt electrodes is 0.4 mm. Before electrophoretic deposition, the sensor substrates were washed with DI water and acetone and then dried. Prior to use, the Pt foil was electrochemically polished in 0.5 M H_2SO_4 by running cyclic voltammograms between 1.1 V and −0.23 V at a scan rate of 0.1 V/s for 50 cycles, followed by washing with DI water and acetone. In a typical deposition, a positive potential was applied to the working electrode (merely immersing the interdigitated electrode part in the Pd NP solution) for 2h. Subsequently, the deposited sensor substrate was taken out from the reaction and dried in air under ambient conditions. In this work, four positive potentials of 1, 2, 5, and 10 V were used to prepare Pd/PdO$_x$ with different oxidation states.

Preparation of other Pd sensing materials. Apart from potential regulation, the composition of the sensing materials was tuned by annealing Pd/PdO$_x$ sensors at 400°C in air for 1, 3, and 6 h using a hotplate (Thermo Scientific). For comparison, the Pd/PdO$_x$ sensors were also heated in Ar at 400°C for 6 h using a Schlenk flask.

1 mg powder of commercial PdO$_X$ (PdO$_x$/C, Sigma Aldrich), Pd black (Pd black/C, Sigma Aldrich), or the mixture of PdO$_X$/Pd black in the molar ratio of 1:1 (PdO$_x$&Pd black/C mixture) were respectively dispersed in 100 μL ethanol to prepare their corresponding slurries. 10 μL of the obtained slurries were drop-casted on the sensor substrate and then dried at ambient air naturally.

Gas sensing tests. The sensing measurements were carried out using a home-built apparatus at room temperature (22°C). Specifically, the test setup consists of four parts: 1) Gas cylinders of synthetic air and high purity of hydrogen (Airgas Co., Ltd); 2) Mass flowrate controllers (MFC, Bronkhorst) for regulating gas flow rates; 3) Data acquisition meter (Keysight/Agilent 34972A LXI) for measuring the electrical resistance in real-time; 4) A PC connected to the meter for recording the resistance data. In a typical H_2 sensing test protocol, the Pd/PdO$_x$ sensors were first stabilized in air for 1 hour at a constant flow rate of 1000 sccm. When the sensors reached a constant electrical resistance of ca. 0.1 MΩ, the desired concentration of H_2 was achieved by varying the flow rate ratio of H_2 and air flowed over the sensors for 5 min, and then removed H_2 from the mixed gas. The total flow rate in this test was maintained at 1000 sccm. The measurements for other interference gases in the selectivity study used the same protocol as H_2. The concentration for most of the interference gases was 4%, except H_2S (0.4 ppm), NO_2 (4 ppm), SO_2 (4 ppm), ethylene (40 ppm). H_2S, NO, NO_2, SO_2, ethylene, and methane were purchased from Airgas Co., Ltd. The

sources of the other interference gases were bought from Sigma Aldrich as high purity of liquids, and their concentrations were adjusted by the flow rate ratio of pure air and air bubbling through corresponding liquids. The relative humidity was calculated by the ratio of wet air (after bubbling through DI water) and dry air.

Material characterization. The surface morphology of the Pd/PdO_x sensors was collected using a JEOL JSM 7600F SEM. A JEOL 3100R05 TEM (Double Cs Corrected TEM/STEM) was utilized to collect high-angle annular dark-field scanning transmission electron microscopy (HAADF-STEM) images for further structural characterization and analysis. The TEM samples were prepared by touching the deposited sensor surface using a TEM grid (carbon-coated 200-mesh Cu grids) to transfer the solid sample to the grid. Since the alumina (relatively strong intensity) and Pt electrode (the peak position relatively close to Pd) from the sensor substrate has obvious interference with the analysis of Pd/PdO_x, Pd NPs were deposited on the carbon papers (FuelCellStore, SKU: 1594008-1) using the same protocol in the powder X-ray diffraction (PXRD) test (Bruker D2 Phaser diffractometer). X-ray diffraction patterns were analyzed by the powder diffraction file database of the International Center for Diffraction Data. X-ray photoelectron spectroscopy (XPS) characterizations were performed using an Al K-alpha X-ray Photoelectron Spectrometer (Thermo Scientific, K-alpha). XPS spectra were fitted by a composite function (30% Lorentzian+70% Gaussian) using Avantage software. All the XPS spectra were calibrated by the position of the C 1s peak at 284.8 eV.

Theoretical calculations. All calculations were performed via the Vienna Ab Initio simulation package utilizing DFT[49, 50]. Core electrons were described using the projected-augmented wave (PAW) method[51]. The Kohn-Sham wave functions were expanded on a plane-wave basis with a kinetic energy cutoff of 400 eV to describe the valence electrons. The generalized gradient approximation using the Perdew-Burke-Ernzerhof functional was employed to evaluate the exchange-correlation energy[52].

The PdO (101) and PdO_2 (110) surfaces were modeled with a four-layer (2×4) PdO(101) supercell and PdO_2 (110) supercell, respectively. The bottom two layers of the surface were kept frozen, while the other layers and adsorbed gas molecules were set free to relax. A vacuum of >14 Å was added to all surface models to ensure no appreciable interaction between periodic images. The Monkhorst-Pack scheme was employed to sample the Brillouin zone using a 3×3×1 k-point grid for atomic structure optimization[53]. The interface of PdO (or PdO_2) supported Pd nanoparticle is modeled by a periodic one-dimensional Pd rod deposited along the [010] direction of a PdO (101) slab (or PdO_2 (110) slab). For Pd/PdO and Pd/PdO_2 models, a vacuum space of >14 Å was added to prevent any appreciable interaction between periodic images. The Brillouin zone was sampled only on Gamma point for geometry optimization. All geometries were considered optimized when the force on each atom was < 0.025 eV/Å. The location and energy of transition states were calculated with the climbing-image nudged elastic band method[54, 55].

Supporting information

The Supporting Information is available free of charge on the ACS Publications website.

Experimental details and XPS results.

AUTHOR INFORMATION

Corresponding Authors

* zhangbright@tsinghua.edu.cn

* long.luo@wayne.edu

Author Contributions

‡These authors contributed equally: Xin Geng and Shuwei Li

Notes

The authors declare no competing financial interest.

ACKNOWLEDGEMENTS

The work at Wayne State University and the Pacific Northwest National Laboratory was supported by the U.S. Department of Energy (DOE), Office of Science, Office of Basic Energy Sciences, through Award # 78705. In addition, L.L. and X. G. acknowledge support from National Science Foundation under award

CHE-1943737. L.Z and S. L acknowledge support from the National Natural Science Foundation of China under grant No. 22103047 and Hefei National Laboratory for Physical Sciences at the Microscale (KF2020107). We also thank Prof. Reg Penner at the University of California, Irvine, for his valuable suggestions.

REFERENCES

1. Hydrogen to the rescue. *Nat. Mater.* **2018,** *17* (7), 565.
2. Koo, W.-T.; Cho, H.-J.; Kim, D.-H.; Kim, Y. H.; Shin, H.; Penner, R. M.; Kim, I.-D., Chemiresistive Hydrogen Sensors: Fundamentals, Recent Advances, and Challenges. *ACS Nano* **2020,** *14* (11), 14284-14322.
3. *U.S. Department of Energy, Energy Efficiency and Renewable Energy (EERE), Fuel Cell Technologies Office. Multi-Year Research, Development, and Demonstration Plan, 2011–2020. Section 3.7 Hydrogen Safety, Codes and Standards (EERE, 2015).*
4. U.S. Department of Energy, Energy Efficiency and Renewable Energy (EERE), Fuel Cell Technologies Office. *Multi-Year Research, Development, and Demonstration Plan, 2011–2020. Section 3.7 Hydrogen Safety, Codes and Standards* **2015**.
5. Bannenberg, L.; Schreuders, H.; Dam, B., Tantalum-Palladium: Hysteresis-Free Optical Hydrogen Sensor Over 7 Orders of Magnitude in Pressure with Sub-Second Response. *Adv. Funct. Mater.* **2021,** *31* (16), 2010483.
6. Behzadi Pour, G.; Fekri Aval, L.; Esmaili, P., Performance of gas nanosensor in 1-4 per cent hydrogen concentration. *Sensor Review* **2019,** *39* (4), 622-628.
7. Chang, T.; Jung, H.; Jang, B.; Lee, J.; Noh, J.-S.; Lee, W., Nanogaps controlled by liquid nitrogen freezing and the effects on hydrogen gas sensor performance. *Sensors and Actuators A: Physical* **2013,** *192*, 140-144.
8. Favier, F.; Walter, E. C.; Zach, M. P.; Benter, T.; Penner, R. M., Hydrogen sensors and switches from electrodeposited palladium mesowire arrays. *Science* **2001,** *293* (5538), 2227-31.
9. Lee, J.; Noh, J.-S.; Lee, S. H.; Song, B.; Jung, H.; Kim, W.; Lee, W., Cracked palladium films on an elastomeric substrate for use as hydrogen sensors. *Int. J. Hydrogen Energy* **2012,** *37* (9), 7934-7939.
10. Nugroho, F. A. A.; Darmadi, I.; Cusinato, L.; Susarrey-Arce, A.; Schreuders, H.; Bannenberg, L. J.; da Silva Fanta, A. B.; Kadkhodazadeh, S.; Wagner, J. B.; Antosiewicz, T. J.; Hellman, A.; Zhdanov, V. P.; Dam, B.; Langhammer, C., Metal-polymer hybrid nanomaterials for plasmonic ultrafast hydrogen detection. *Nat. Mater.* **2019,** *18* (5), 489-495.
11. Sirbuly, D. J.; Létant, S. E.; Ratto, T. V., Hydrogen Sensing with Subwavelength Optical Waveguides via Porous Silsesquioxane-Palladium Nanocomposites. *Adv. Mater. (Weinheim, Ger.)* **2008,** *20* (24), 4724-4727.
12. Xu, T.; Zach, M. P.; Xiao, Z. L.; Rosenmann, D.; Welp, U.; Kwok, W. K.; Crabtree, G. W., Self-assembled monolayer-enhanced hydrogen sensing with ultrathin palladium films. *Appl. Phys. Lett.* **2005,** *86* (20), 203104.
13. Luong, H. M.; Pham, M. T.; Guin, T.; Madhogaria, R. P.; Phan, M.-H.; Larsen, G. K.; Nguyen, T. D., Sub-second and ppm-level optical sensing of hydrogen using templated control of nano-hydride geometry and composition. *Nat. Commun.* **2021,** *12* (1), 2414.
14. Darmadi, I.; Nugroho, F. A. A.; Kadkhodazadeh, S.; Wagner, J. B.; Langhammer, C., Rationally Designed PdAuCu Ternary Alloy Nanoparticles for Intrinsically Deactivation-Resistant Ultrafast Plasmonic Hydrogen Sensing. *ACS Sensors* **2019,** *4* (5), 1424-1432.
15. Lee, J.; Shim, W.; Lee, E.; Noh, J. S.; Lee, W., Highly mobile palladium thin films on an elastomeric substrate: Nanogap-based hydrogen gas sensors. *Angew. Chem., Int. Ed.* **2011,** *50* (23), 5301-5305.
16. Koo, W.-T.; Qiao, S.; Ogata, A. F.; Jha, G.; Jang, J.-S.; Chen, V. T.; Kim, I.-D.; Penner, R. M., Accelerating Palladium Nanowire H2 Sensors Using Engineered Nanofiltration. *ACS Nano* **2017,** *11* (9), 9276-9285.
17. Yamazoe, N., Toward innovations of gas sensor technology. *Sens. Actuators B: Chem.* **2005,** *108* (1), 2-14.
18. Rukini, A.; Rhamdhani, M. A.; Brooks, G. A.; Van den Bulck, A., Metals Production and Metal Oxides Reduction Using Hydrogen: A Review. *Journal of Sustainable Metallurgy* **2022,** (8), 1-24.

19. Kim, J. Y.; Rodriguez, J. A.; Hanson, J. C.; Frenkel, A. I.; Lee, P. L., Reduction of CuO and Cu2O with H2: H Embedding and Kinetic Effects in the Formation of Suboxides. *J. Am. Chem. Soc.* **2003,** *125* (35), 10684-10692.
20. Su, S. C.; Carstens, J. N.; Bell, A. T., A Study of the Dynamics of Pd Oxidation and PdO Reduction by H2and CH4. *J. Catal.* **1998,** *176* (1), 125-135.
21. O'Connor, C. R.; van Spronsen, M. A.; Egle, T.; Xu, F.; Kersell, H. R.; Oliver-Meseguer, J.; Karatok, M.; Salmeron, M.; Madix, R. J.; Friend, C. M., Hydrogen migration at restructuring palladium-silver oxide boundaries dramatically enhances reduction rate of silver oxide. *Nat. Commun.* **2020,** *11* (1), 1844.
22. Manukyan, K. V.; Avetisyan, A. G.; Shuck, C. E.; Chatilyan, H. A.; Rouvimov, S.; Kharatyan, S. L.; Mukasyan, A. S., Nickel Oxide Reduction by Hydrogen: Kinetics and Structural Transformations. *J. Phys. Chem. C* **2015,** *119* (28), 16131-16138.
23. Martin, N. M.; Van den Bossche, M.; Grönbeck, H.; Hakanoglu, C.; Gustafson, J.; Blomberg, S.; Arman, M. A.; Antony, A.; Rai, R.; Asthagiri, A.; Weaver, J. F.; Lundgren, E., Dissociative Adsorption of Hydrogen on PdO(101) Studied by HRCLS and DFT. *J. Phys. Chem. C* **2013,** *117* (26), 13510-13519.
24. Bliem, R.; van der Hoeven, J.; Zavodny, A.; Gamba, O.; Pavelec, J.; de Jongh, P. E.; Schmid, M.; Diebold, U.; Parkinson, G. S., An Atomic-Scale View of CO and H2 Oxidation on a Pt/Fe3 O4 Model Catalyst. *Angew. Chem. Int. Ed.* **2015,** *54* (47), 13999-4002.
25. Brown, M. K.; Degrado, S. J.; Hoveyda, A. H., Highly enantioselective Cu-catalyzed conjugate additions of dialkylzinc reagents to unsaturated furanones and pyranones: preparation of air-stable and catalytically active Cu-peptide complexes. *Angew. Chem. Int. Ed.* **2005,** *44* (33), 5306-10.
26. Carrettin, S.; Concepcion, P.; Corma, A.; Lopez Nieto, J. M.; Puntes, V. F., Nanocrystalline CeO2 increases the activity of Au for CO oxidation by two orders of magnitude. *Angew. Chem. Int. Ed.* **2004,** *43* (19), 2538-40.
27. Falsig, H.; Hvolbaek, B.; Kristensen, I. S.; Jiang, T.; Bligaard, T.; Christensen, C. H.; Norskov, J. K., Trends in the catalytic CO oxidation activity of nanoparticles. *Angew. Chem. Int. Ed.* **2008,** *47* (26), 4835-9.
28. Remediakis, I. N.; Lopez, N.; Norskov, J. K., CO oxidation on rutile-supported au nanoparticles. *Angew. Chem. Int. Ed.* **2005,** *44* (12), 1824-6.
29. Rodriguez, J. A.; Graciani, J.; Evans, J.; Park, J. B.; Yang, F.; Stacchiola, D.; Senanayake, S. D.; Ma, S.; Perez, M.; Liu, P.; Fdez Sanz, J.; Hrbek, J., Water-gas shift reaction on a highly active inverse CeOx/Cu111 catalyst: unique role of ceria nanoparticles. *Angew. Chem. Int. Ed.* **2009,** *48* (43), 8047-50.
30. Ruiz Puigdollers, A.; Schlexer, P.; Tosoni, S.; Pacchioni, G., Increasing Oxide Reducibility: The Role of Metal/Oxide Interfaces in the Formation of Oxygen Vacancies. *ACS Catal.* **2017,** *7* (10), 6493-6513.
31. Shao, X.; Prada, S.; Giordano, L.; Pacchioni, G.; Nilius, N.; Freund, H. J., Tailoring the shape of metal ad-particles by doping the oxide support. *Angew. Chem. Int. Ed.* **2011,** *50* (48), 11525-7.
32. Sterrer, M.; Yulikov, M.; Fischbach, E.; Heyde, M.; Rust, H. P.; Pacchioni, G.; Risse, T.; Freund, H. J., Interaction of gold clusters with color centers on MgO(001) films. *Angew. Chem. Int. Ed.* **2006,** *45* (16), 2630-2.
33. Sun, Y. N.; Giordano, L.; Goniakowski, J.; Lewandowski, M.; Qin, Z. H.; Noguera, C.; Shaikhutdinov, S.; Pacchioni, G.; Freund, H. J., The interplay between structure and CO oxidation catalysis on metal-supported ultrathin oxide films. *Angew. Chem. Int. Ed.* **2010,** *49* (26), 4418-21.
34. Widmann, D.; Behm, R. J., Active oxygen on a Au/TiO2 catalyst: formation, stability, and CO oxidation activity. *Angew. Chem. Int. Ed.* **2011,** *50* (43), 10241-5.
35. Khoobiar, S., Particle to Particle Migration of Hydrogen Atoms on Platinum-Alumina Catalysts from Particle to Neighboring Particles. *J. Phys. Chem.* **1964,** *68*, 411.
36. Prins, R., Hydrogen spillover. Facts and fiction. *Chem. Rev.* **2012,** *112* (5), 2714-38.
37. Schilling, A. C.; Groden, K.; Simonovis, J. P.; Hunt, A.; Hannagan, R. T.; Çınar, V.; McEwen, J.-S.; Sykes, E. C. H.; Waluyo, I., Accelerated Cu2O Reduction by Single Pt Atoms at the Metal-Oxide Interface. *ACS Catal.* **2020,** *10* (7), 4215-4226.
38. Huang, W.; Johnston-Peck Aaron, C.; Wolter, T.; Yang Wei-Chang, D.; Xu, L.; Oh, J.; Reeves Benjamin, A.; Zhou, C.; Holtz Megan, E.; Herzing Andrew, A.; Lindenberg Aaron, M.; Mavrikakis,

M.; Cargnello, M., Steam-created grain boundaries for methane C–H activation in palladium catalysts. *Science* **2021,** *373* (6562), 1518-1523.
39. Hickling, A.; Vrjosek, G. G., Anodic oxidation of palladium. *Transactions of the Faraday Society* **1961,** *57* (0), 123-129.
40. Garche, J.; Dyer, C.; Moseley, P. T.; Ogumi, Z.; Rand, D. A. J.; Scrosati, B., *Encyclopedia of Electrochemical Power Sources*. Elsevier Science: 2013.
41. Chin, Y.-H.; Buda, C.; Neurock, M.; Iglesia, E., Consequences of Metal–Oxide Interconversion for C–H Bond Activation during CH4 Reactions on Pd Catalysts. *J. Am. Chem. Soc.* **2013,** *135* (41), 15425-15442.
42. Gabasch, H.; Knop-Gericke, A.; Schlögl, R.; Borasio, M.; Weilach, C.; Rupprechter, G.; Penner, S.; Jenewein, B.; Hayek, K.; Klötzer, B., Comparison of the reactivity of different Pd–O species in CO oxidation. *Phys. Chem. Chem. Phys.* **2007,** *9* (4), 533-540.
43. Kim, H.-J.; Lee, J.-H., Highly sensitive and selective gas sensors using p-type oxide semiconductors: Overview. *Sens. Actuators B: Chem.* **2014,** *192*, 607-627.
44. Rogers, D. B.; Shannon, R. D.; Gillson, J. L., Crystal growth and semiconductivity of palladium oxide. *J. Solid State Chem.* **1971,** *3* (2), 314-316.
45. Cho, H.-J.; Chen, V. T.; Qiao, S.; Koo, W.-T.; Penner, R. M.; Kim, I.-D., Pt-Functionalized PdO Nanowires for Room Temperature Hydrogen Gas Sensors. *ACS Sensors* **2018,** *3* (10), 2152-2158.
46. Belousov, V. M.; Vasylyev, M. A.; Lyashenko, L. V.; Vilkova, N. Y.; Nieuwenhuys, B. E., The low-temperature reduction of Pd-doped transition metal oxide surfaces with hydrogen. *Chem. Eng. J.* **2003,** *91* (2), 143-150.
47. Gao, Z.; Wang, T.; Li, X.; Li, Q.; Zhang, X.; Cao, T.; Li, Y.; Zhang, L.; Guo, L.; Fu, Y., Pd-Decorated PdO Hollow Shells: A H2-Sensing System in Which Catalyst Nanoparticle and Semiconductor Support are Interconvertible. *ACS Appl. Mater. Interfaces* **2020,** *12* (38), 42971-42981.
48. Yang, S.; Li, Q.; Li, C.; Cao, T.; Wang, T.; Fan, F.; Zhang, X.; Fu, Y., Enhancing the Hydrogen-Sensing Performance of p-Type PdO by Modulating the Conduction Model. *ACS Appl. Mater. Interfaces* **2021,** *13* (44), 52754-52764.
49. Kresse, G.; Hafner, J., Ab initio molecular dynamics for liquid metals. *Physical Review B* **1993,** *47* (1), 558.
50. Kresse, G.; Furthmüller, J., Efficiency of ab-initio total energy calculations for metals and semiconductors using a plane-wave basis set. *Computational materials science* **1996,** *6* (1), 15-50.
51. Kresse, G.; Joubert, D., From ultrasoft pseudopotentials to the projector augmented-wave method. *Physical review b* **1999,** *59* (3), 1758.
52. Perdew, J. P.; Burke, K.; Ernzerhof, M., Generalized gradient approximation made simple. *Physical review letters* **1996,** *77* (18), 3865.
53. Monkhorst, H. J.; Pack, J. D., Special points for Brillouin-zone integrations. *Physical review B* **1976,** *13* (12), 5188.
54. Henkelman, G.; Uberuaga, B. P.; Jónsson, H., A climbing image nudged elastic band method for finding saddle points and minimum energy paths. *The Journal of chemical physics* **2000,** *113* (22), 9901-9904.
55. Henkelman, G.; Jónsson, H., Improved tangent estimate in the nudged elastic band method for finding minimum energy paths and saddle points. *The Journal of chemical physics* **2000,** *113* (22), 9978-9985.

TOC graphics